Nanoarchitectonics of Bacterial Cellulose with Nickel-Phosphorous Alloy as a Binder-Free Electrode for Efficient Hydrogen Evolution Reaction in Neutral Solution

Wenhai Wang,[a] Siavash Khabazian,[b] Marina Casas Papiol,[a] Soledad Roig-Sanchez,[a] Anna Laromaine,[a] Anna Roig,[a] Dino Tonti [a*]

[a] Institut de Ciència de Materials de Barcelona (ICMAB), CSIC, Campus UAB, Bellaterra, Spain

[b] Nanomaterials Group, Department of Materials Science and Engineering, Tarbiat Modares University, Tehran, Iran

* Corresponding authors.

E-mail addresses: dino.t@csic.es (D. Tonti).

Abstract

Developing low-cost and efficient electrodes for hydrogen evolution reaction (HER) under neutral electrolytes remains an unattained milestone. We report a highly performing binder-free electrode through electroless deposition of Ni-P nanoparticles on bacterial cellulose (BC). Not needing carbonization to provide the electric conductivity, BC can maintain its excellent mechanical properties and thin fiber microstructure. The nanometric cellulose fibers facilitate the formation of small Ni-P nanoparticles, leading to more catalytic active sites. The obtained Ni-P/BC electrode presents remarkable HER activity with an overpotential of only 161 mV at 10 mA cm^{-2} and a low Tafel slope (141 mV dec^{-1}) in 1 M potassium phosphate-buffered saline (pH=7) electrolyte. Besides, Ni-P/BC also exhibits good stability for 24 h at 10

23 mA cm^{-2}. This binder-free, low-cost, and easily fabricated electrode holds excellent

24 promise for HER applications in benign neutral environments.

27

1. Introduction

29   The consumption of fossil fuels and the climate changes urge the constant

30 development of renewable energy solutions [1, 2]. Among technologies used for

31 renewable energy production, electrochemical hydrogen evolution reaction (HER) to

32 obtain hydrogen sustainably has drawn remarkable attention due to the high efficiency

33 of producing H$_2$, according to reactions ($2H^+ + 2e^- \rightarrow H_2$ or $2H_2O + 2e^- \rightarrow H_2 + 2OH^-$

34 depending on the pH) [3, 4]. However, the slow kinetics degrades the performance of

35 HER [5, 6], requiring an appropriate catalyst. It is known that platinum-based

36 catalysts exhibit the most effective HER activity [7], while the high cost and low

37 abundance of Pt hinder its widespread application [8, 9]. To date, advances have been

38 made in developing a series of non-precious metal-based catalysts [10-12].

39 Additionally, HER is mainly carried out in either acidic or alkaline electrolytes [13],

40 inevitably contributing to cell component corrosion issues and environmental hazards

41 that hamper large-scale applications. Currently, only rare or noble metals present

42 remarkable HER performance in neutral electrolytes, where large ohmic loss and slow

43 kinetics are typical [14]. In fact, HER in neutral solutions usually demands much

44 larger overpotentials to reach a similar current as in acid or alkaline conditions [15].

45 Consequently, exploring low-cost catalysts with improved HER activity in neutral

46 solutions is highly desired but challenging.

47 Bacterial cellulose (BC), produced from microbial fermentation, has emerged as

48 a promising bio-based material in energy conversion and storage thanks to its

49 relatively low cost, eco-friendliness and 3D porous structure [16, 17]. BC has been

50 reported to prepare HER catalysts. On account of the insulating character of BC, BC

51 is usually carbonized to improve the electrode's conductivity [18-22]. Nevertheless,

52 carbonized BC often loses the original excellent mechanical properties of BC and

53 becomes fragile [23]. Hence, catalysts based on carbonized BC are usually

54 immobilized on conductive substrates with the help of binders, impacting negatively

55 on the electrochemically active sites [24]. Therefore, it is challenging to develop

56 pristine BC-based electrodes with high HER performance.

57 Given these considerations, here we report a facile and low-cost method to

58 fabricate a freestanding electrode by in situ growing Ni-P on BC by electroless

59 deposition (ELD) for HER [25]. Considering the high conductivity and the high HER

60 activity of nickel-phosphorous (Ni-P) alloys [26, 27], pristine BC with remarkable

61 mechanical properties was integrated with Ni-P by ELD. The prepared Ni-P/BC

62 possesses the properties of Ni-P and BC at the same time. As a consequence, Ni-P/BC

63 can be employed as a HER electrode directly. In addition, the method to fabricate in

64 situ Ni-P on BC removes any need for binders. In this case, BC not only acts as a

65 substrate for the growth of Ni-P particles but also the thin cellulose fibers (20-100 nm)

66 of BC are beneficial to form small nanoparticles [28], resulting in a large number of

67 electrocatalytic active sites. This simple strategy based on non-carbonized, pristine

68 BC to obtain small nanoparticles is more effective than traditional ways using

69 end-capping reagents or expensive organic precursors [29-31]. In comparison,

70 microfibrillated substrates (such as filter paper or glass fiber paper) can generate

71 larger Ni-P particles. Moreover, Ni-P/BC exhibits superior HER performance with a

72 remarkably small overpotential of 161 mV at 10 mA cm^{-2} and a low Tafel slope (141

73 mV dec^{-1}) in a neutral solution. Besides, Ni-P/BC demonstrates stronger stability than

74 commercial Pt/C. The mild experimental conditions, the straightforward fabrication

75 and the excellent HER performance make Ni-P/BC electrode a strong candidate for

76 practical applications.

77

78 **2. Materials and methods**

79 *2.1 Materials*

80 Food-grade bacterial cellulose (Q-Phil Products International) was bought from an

81 Asian food store. Nickel sulfate hexahydrate (NiSO$_4$·6H$_2$O, 98 %), Sodium citrate

82 dihydrate (Na$_3$C$_6$H$_5$O$_7$·2H$_2$O, 99 %), dimethylamine-borane (DMAB, 97 %) and

83 palladium dichloride (PdCl$_2$, 99.9 %) were purchased from Alfa Aesar. Ammonium

84 chloride (NH$_4$Cl, 99.5 %), sodium borohydride (NaBH$_4$, 99 %), cobalt (II) sulfate

85 heptahydrate (CoSO$_4$·5H$_2$O, 99 %) and Nafion 117 containing solution (5 %) were

86 bought from Sigma. Tin chloride dihydrate (SnCl$_2$·2H$_2$O, > 99%), dipotassium

87 hydrogenphosphate (K$_2$HPO$_4$, ≥ 99 %), potassium dihydrogen phosphate (KH$_2$PO$_4$, ≥

88 99.5%) and face mask (FPP2) were supplied from Labkem. Ethanol (99 %) was

89   purchased from Panreac. Hydrogen chloride (HCl, 37 %) was bought from Scharlab.

90   Ammonia solution (NH_3, 30 %) was purchased from Panreac. Sodium hypophosphite

91   monohydrate ($NaH_2PO_2 \cdot H_2O$) was bought from Acros Organics. Pt/C (20 %) and

92   carbon paper (Freudenberg H2315, 210 μm thick) were obtained from QuinTech.

93   *2.2 Electrodes Preparation*

94   Commercial BC was washed with MilliQ water to remove the absorbed syrup. After

95   that, it was autoclaved and treated with ethanol as described previously [32]. Briefly,

96   the purified BC was squeezed under ~150 g Teflon cylinder for 10 min to remove

97   most water and the pressed BC was placed in ethanol and kept stirring for 2 h at room

98   temperature. Then the ethanol-treated BC was dried in an oven (60 °C, 24 h). Dried

99   BC was sensitized by immersing in an Sn^{2+} solution (0.05 M $SnCl_2$, 0.12 M HCl) for

100   30 min to absorb Sn^{2+} ions on the surface and washed in Milli-Q water 3 times. Next,

101   BC was soaked in a Pd^{2+} solution (100 μg mL^{-1} $PdCl_2$, 0.03 M HCl) for 30 min and

102   again rinsed in Milli-Q water 3 times. The reaction between Sn^{2+} and Pd^{2+} generates

103   Pd particles that will catalyze the Ni deposition [33]. Finally, a 20 mL electroless

104   deposition (ELD) solution (2 mmol $NiSO_4 \cdot 6H_2O$, 2 mmol $Na_3C_6H_5O_7 \cdot 2H_2O$, 2 mmol

105   NaH_2PO_2 and 14 mmol NH_4Cl) was adjusted by ammonia solution to a pH of 8 and

106   heated to 60 °C. The BC was dipped in the bath and kept for 10 min and after that,

107   washed in Milli-Q water and ethanol 3 times. The washed BC was dried in Argon (Ar)

108   atmosphere. The electrode was labeled as Ni-P/BC.

109    $NaBH_4$ and DMAB were also used as alternative Ni reducing agents. Due to the

110   strong reducing ability of $NaBH_4$, 5 mL fresh $NaBH_4$ solution was added dropwise to

111   the ELD solution. DMAB was instead used in the same manner as NaH_2PO_2. The

112   electrodes derived from $NaBH_4$ and DMAB were respectively labeled as Ni-B-1/BC

113   and Ni-B-2/BC.

114   Filter paper (FP) and glass fiber paper (GFP) were also used as substrates to

115   prepare Ni-P using the same method as with BC. The obtained electrodes were labeled

116   as Ni-P/FP and Ni-P/GFP.

117   A series of Ni-Co-P/BC electrodes were also synthesized by changing the molar

118   ratios of Ni^{2+} and Co^{2+} (Ni/Co=8/2; 5/5; 2/8) in the electroless plating solution. The

119   corresponding electrodes are separately denoted as Ni-Co-P-1/BC, Ni-Co-P-2/BC and

120   Ni-Co-P-3/BC. Co-P/BC was obtained with 2 mmol $CoSO_4·5H_2O$ in the same way as

121   Ni-P/BC.

122   For comparisons, a Pt/C electrode was prepared by dispersing 5 mg Pt/C (20

123   wt %) in the mixture made of 30 μL Nafion solution + 970 μL ethanol [34]. Then the

124   dispersion was treated by ultrasound for 1 min to form an ink that was dropped on

125   carbon paper to obtain a loading of 5.0 mg cm^{-2}.

126   *2.3 Characterization*

127   Scanning Electron Microscopy (SEM) images to investigate the surface morphology

128   and the size of samples were recorded by FEI Quanta 200 FEG-ESEM equipment

129   operating at 10 kV. SEM samples were attached to an aluminum holder by adhesive

130   carbon tape. Images were analyzed with ImageJ [35] to estimate fiber and particle

131   diameters. Transmission electron microscopy (TEM) images were performed to

132   observe the morphology and the size of samples using JEOL JEM1210 TEM at 120

133 kV. Tiny amounts of Ni-P or Ni-B were detached from BC in ethanol by ultrasonic

134 treatment for 1 min. The dispersions were sonicated again for about 30 s and then

135 dropped on carbon-coated copper grids for TEM measurement. X-ray diffraction

136 (XRD) patterns were carried out to confirm the crystal phase of samples on a Siemens

137 D-5000 equipment with Cu Kα radiation. X-ray Photoelectron Spectroscopy (XPS)

138 measurements to determine the chemical state of samples were performed on a

139 SPECS EA10P hemispherical analyzer with a monochromatic Al Kα source.

140 *2.4 Electrochemical measurements*

141 The electrochemical measurements were carried out in a three-electrode cell by a

142 Bio-logic VMP3 multichannel potentiostat. Graphite rod, Ag/AgCl electrode and

143 prepared electrodes (1x1 cm) were respectively used as the counter electrode, the

144 reference electrode and the working electrode. The potentials (V *vs* Ag/AgCl)

145 measured in this work were converted to the potentials of reversible hydrogen

146 electrode (RHE) according to the following equation $E_{RHE}=E_{Ag/AgCl}+0.197+0.059pH$

147 [36]. All electrochemical measurements were performed in N_2 saturated 1 M

148 potassium phosphate-buffered saline (PBS, pH=7) electrolyte. Polarization curves and

149 Tafel plots were elaborated from linear sweep voltammetry (LSV) conducted with a

150 scan rate of 10 mV s^{-1}. All LSV curves were corrected for iR drop. Electrochemical

151 impedance spectroscopy (EIS) measurements were tested in the frequency range from

152 100 kHz to 0.01 Hz with 5 mV amplitude. The double-layer capacitance (C_{dl}) was

153 measured by cyclic voltammetry (CV) at different scan rates (20-100 mV s^{-1}).

154

3. Results and discussion
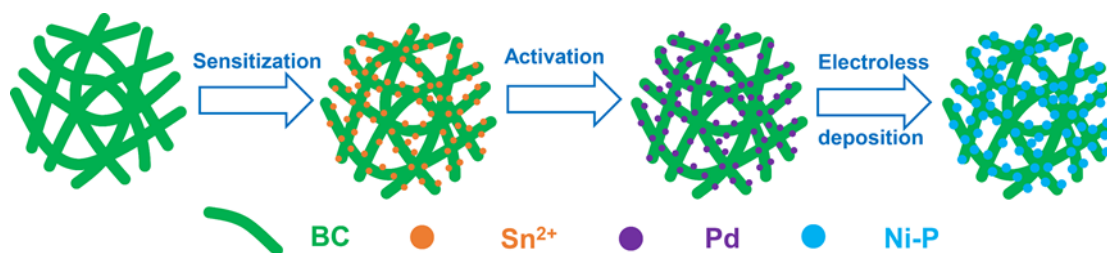
**Figure 1.** Schematic illustration of the synthesis routine of Ni-P/BC.

Figure 1 schematically illustrates the preparation of Ni-P on BC by ELD. The starting cellulose after purification is soaked in alcohol before drying. As shown previously [35] this treatment allows retaining a large porosity after drying in contrast to direct drying from water. Alcohol-dried cellulose is then soaked again in the three subsequent baths necessary for the ELD process: sensitization with $SnCl_2$, activation with $PdCl_2$, and finally the Ni-P deposition itself using NaH_2PO_2, $NaBH_4$ or DMAB as Ni reducing agent. All three reducing agents produce spherical particles on BC surface (Figure 2a-c and Figure S1a-c). It can be seen that the particle size of Ni-B-2 (0.1-1 μm) is much larger than for Ni-B-1 (0.05-0.2 μm) and Ni-P (0.1-0.2 μm). Instead, the Ni mass loading using $NaBH_4$ is much lower (0.8 mg cm^{-2}) than the ones with NaH_2PO_2 (5.0 mg cm^{-2}) or DMAB (6.0 mg cm^{-2}). Probably because $NaBH_4$ is a stronger reducing agent and the Ni deposition took place preferentially in the solution rather than on the substrate [37]. In this case, the plating solution turned dark quickly contrasting with the other reducing agents where this happened only towards the end of the deposition time. The rings of selected area electron diffraction (SAED) patterns for Ni-B-1 are more diffuse than Ni-B-2 and Ni-P, confirming the weaker crystallinity of Ni-B-1. Energy-dispersive X-ray spectroscopy (EDS) confirms the presence of Ni,

175 P or B elements (Figure S2). In addition, EDS mapping of Ni-P/BC further confirms

176 that the Ni and P elements are uniformly distributed (Figure 2d).
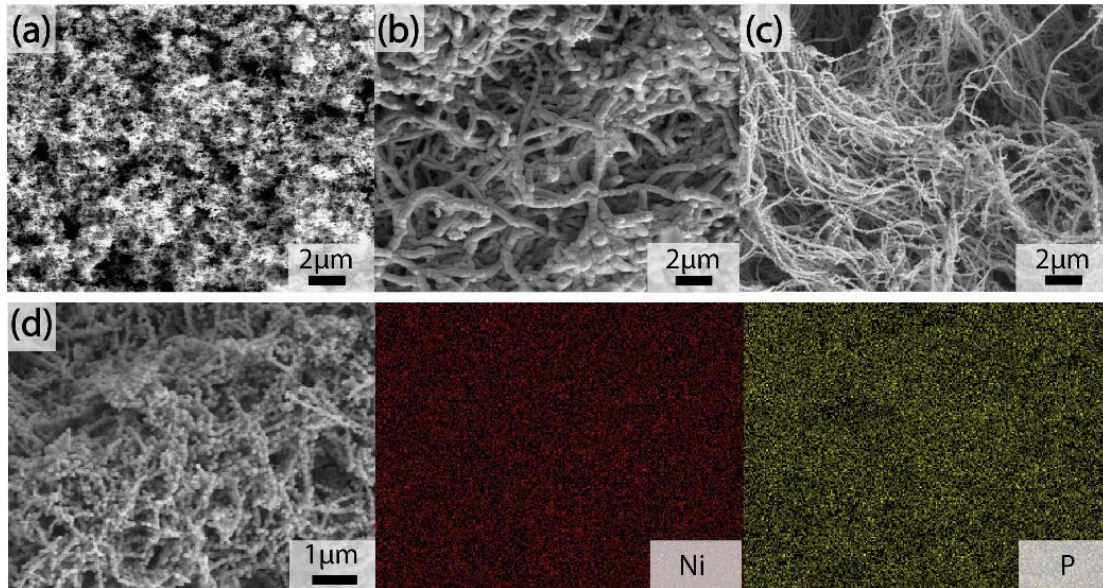
Figure 2. SEM images of (a) Ni-B-1/BC, (b) Ni-B-2/BC, (c) Ni-P/BC. (d) EDS mapping images of Ni-P/BC.

179 The phases and the crystal structures of these samples were evaluated by X-ray

180 diffraction (XRD). The diffraction peaks of bare BC centered at 14.5 ° and 22.5 °

181 belong to the (100) and (110) lattice planes of cellulose (Figure 3a) [38]. For

182 Ni-B-1/BC, only the cellulose peaks are observed, consistent with the low mass of

183 Ni-B-1 on BC and the indication that electroless deposition barely occurred on the BC.

184 In contrast, Ni-P/BC and Ni-B-2/BC present a diffraction peak at $2\Theta=45^{o}$, which can

185 be assigned to the (111) plane of the Ni face-centered cubic structure (JCPDS

186 01-1260). Previous reports indicated that highly crystalline Ni tends to form when the

187 content of B or P is low [39, 40].

188
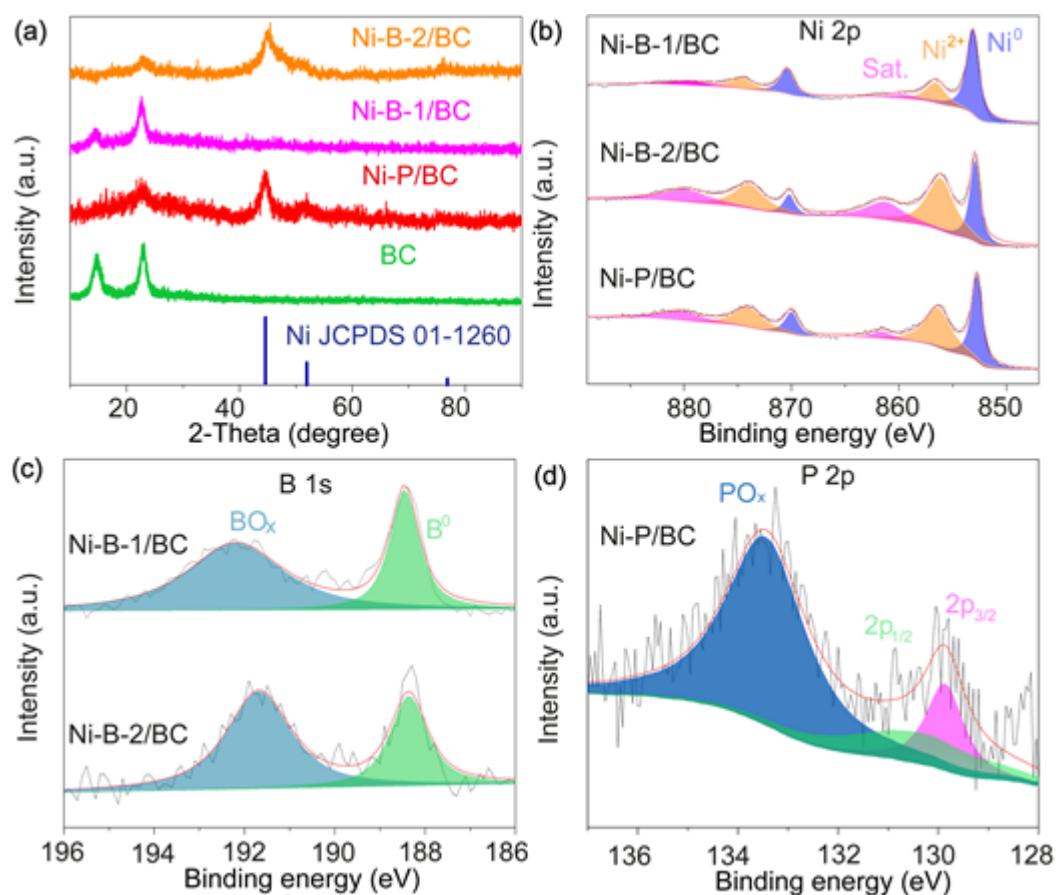
Figure 3. XRD patterns of samples and positions of Ni metal reference (a). XPS spectra and fitting of Ni 2p (b). B

190   1s (c), and P 2p core levels (d).

191   The results of X-ray photoelectron spectroscopy (XPS) spectra confirm the

192   presence of Ni, B or P elements on the surface of Ni-based BCs, in agreement with

193   EDS results. The binding energies of Ni 2p spectra for all samples, at 870 eV and 853

194   eV, can be attributed to the $2p_{1/2}$ and $2p_{3/2}$ peaks of metallic Ni (Figure 3b and Table

195   S1) [41, 42]. The peaks at 874 eV and 856 eV correspond to Ni^{2+}, which can be

196   assigned to an oxidized state of Ni because of the air exposure [43]. The other two

197   peaks at 861 eV and 880 eV are satellite signals [44]. For Ni-B-1 and Ni-B-2, the

198   deconvolution of B 1s spectrum exhibits two peaks at 188 eV and 192 eV (Figure 3c

199   and Table S2), associated with zero valence B and oxidized B corresponding to

200 surface B_2O_3 [45]. Compared with pure B (187.1 eV) [46], the binding energies of B

201 change positively (Ni-B-1: 188.5 eV; Ni-B-2: 188.4 eV). This suggests some partial

202 electron transfer from B^0 to Ni^0 clusters with consequent dipole formation. This agrees

203 with literature showing that B tends to donate electrons to the metal atoms. [47, 48]. It

204 is worthy to note that compared with pure Ni ($2p_{3/2}$: 853.0 eV) [49], there is instead

205 no significant shift of the Ni spectrum in the Ni-B/BC, probably because the atomic

206 weight of Ni is several times larger than that of B [50]. The P 2p spectra for Ni-P/BC

207 could be deconvoluted into 3 peaks (Figure 3d). The two signals located at 130.4 eV

208 and 129.9 eV can be ascribed to P $2p_{1/2}$ and $2p_{3/2}$ [51]. In comparison with pure P

209 ($2p_{3/2}$:130.2 eV), the binding energy of the P spectrum in this case shifts negatively,

210 indicating that there is partial electron transfer from Ni to P [52]. The negatively

211 charged P is beneficial to accept positively charged protons during the electrocatalytic

212 process [53]. The last signal at about 133.4 eV is attributed to phosphate due to the

213 atmospheric oxidation [54].
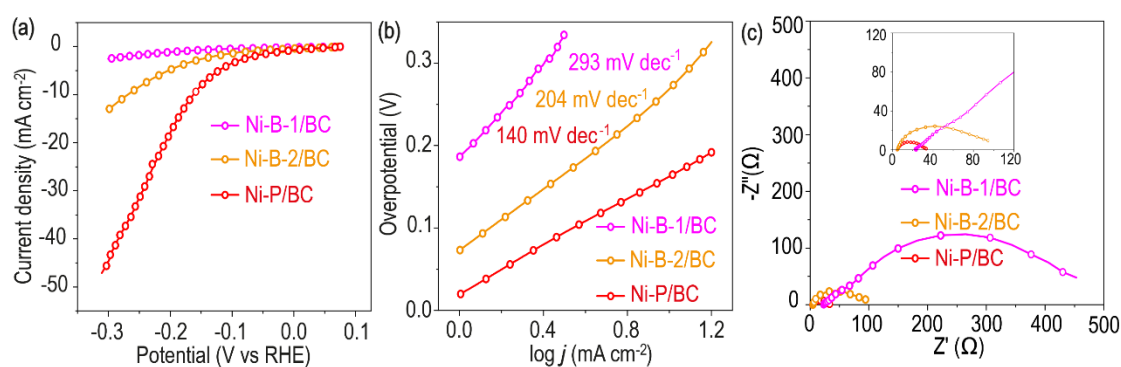
214

215 **Figure 4**. (a) HER polarization curves and (b) corresponding Tafel plots of electrodes in 1 M PBS. (c)
216 Electrochemical impedance spectra of electrodes for different reducing agents at 150 mV overpotential.

217   The electrochemical performance of these electrodes for HER was evaluated in 1

218 M PBS (pH=7) by a three-electrode system. Ni-B-1/BC shows a low reducing current

219 (Figure 4a), demonstrating poor HER performance. Probably it can be attributed to

220 both the poor electric conductivity of Ni-B-1/BC and the low Ni loading of Ni-B-1.

221 Ni-P/BC delivers a much lower overpotential (161 mV) than Ni-B-2/BC (269 mV) at

222 10 mA cm^{-2}. There are two main reasons behind it. On one hand, as indicated by XPS

223 results, B partially transfers electrons to Ni, making the Ni atom in the Ni-B-2/BC

224 electron-rich compared to the Ni-P/BC. Electron-deficient Ni centers favor the

225 hydrogen dissociative chemisorption better than electron-rich Ni ones [49]. On the

226 other hand, the particle size of Ni-P (0.1-0.2 μm) is smaller than Ni-B-2 (0.1-1 μm),

227 which can then provide a larger active surface area resulting in a larger number of

228 active sites [55, 56]. HER kinetics of these electrodes were quantified by Tafel plots.

229 As shown in Figure 4b, Ni-P/BC has a lower Tafel slope than Ni-B-1/BC and

230 Ni-B-2/BC, revealing faster HER kinetics. Electrochemical impedance spectroscopy

231 (EIS) is also useful to evaluate the kinetics of these electrodes. The charge-transfer

232 resistance (R_{ct}) is related to the HER kinetic rate and a lower value implies faster

233 kinetics [57, 58]. Nyquist plots of electrochemical impedance for the three catalysts

234 are presented in Figure 4c. The semicircle diameter corresponds to R_{ct}, and clearly,

235 Ni-P/BC exhibits a smaller R_{ct} than both Ni-B-1/BC and Ni-B-2/BC. This reflects a

236 smaller charge-transfer resistance or a faster charge-transfer kinetics for Ni-P/BC. In

237 addition, as shown by the fitted values in Table S3, the onset on the real axis indicates

238 a larger series resistance for Ni-B-1/BC (23.1 Ω) than Ni-B-2/BC (4.5 Ω) and

239 Ni-P/BC (4.7 Ω), confirming the poor conductivity of Ni-B-1/BC. Next, the effect of

240 Ni-P deposition time on the HER performance was also assessed. As the electroless

241   deposition time extends, the size of Ni-P particles becomes larger (10 min: 0.1-0.2 µm;

242   20 min: 0.1-0.3 µm; 30 min: 0.2-0.7 µm) and the aggregation of Ni-P becomes more

243   obvious (Figure S4), leading to higher overpotentials (Figure S5). Nevertheless, even

244   if the particle size of Ni-P becomes comparable to Ni-B of Ni-B-2/BC, the

245   overpotential remains smaller, confirming the important role of the P doping of Ni.

246   To explore the influence of fiber's diameter on the produced Ni-P, filter paper

247   (FP) and glass fiber paper (GFP) were used as substrates. As shown in Figure S6, the

248   fibers of BC (0.06±0.02 µm) are much thinner than those of FP (18.3 ±3.9 µm) and

249   GFP (0.88±0.38 µm). After ELD (Figure 5a-c and Figure S7), the sizes of Ni-P

250   particles on FP (0.80±0.12 µm) and GFP (0.55±0.17 µm) are much larger than Ni-P

251   particles grown BC (0.18 ±0.04 µm). Besides, the aggregation of Ni-P particles is

252   more critical on FP and GFP. This confirms that the thickness of fibers plays a

253   significant role in the size of Ni-P particles [59]. Despite different substrates and

254   particle sizes, XRD and XPS show similar results (Figure S8-9 and Tables S4-5).
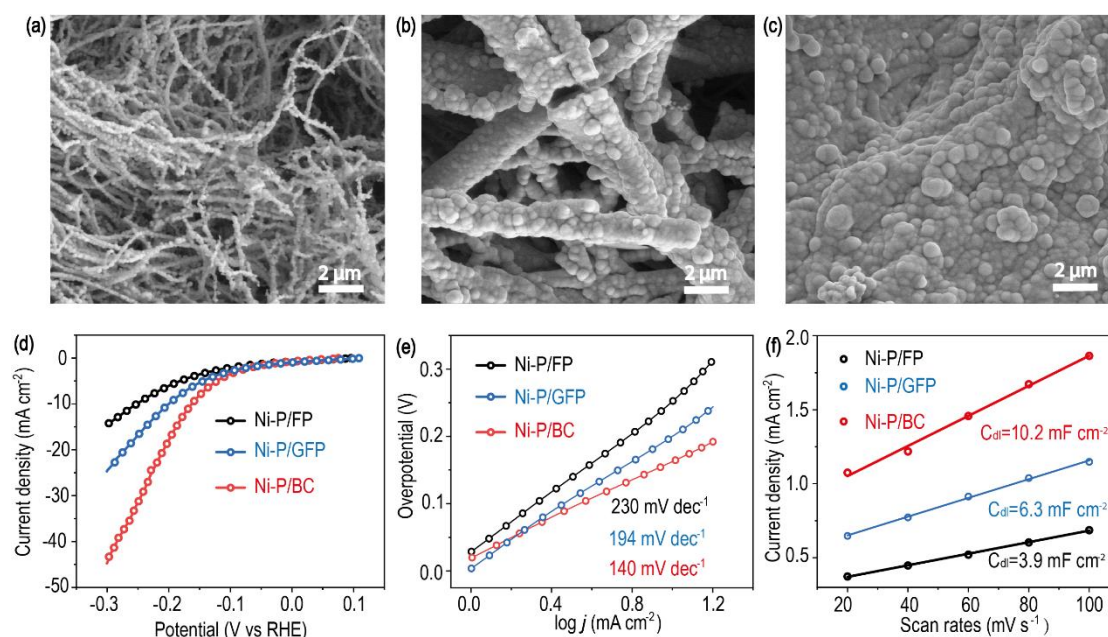
255

259   As shown in the HER polarization curves (Figure 5d), Ni-P/BC presents a lower

260 overpotential (161 mV) than Ni-P/FP (252 mV) and Ni-P/GFP (201 mV) at 10 mA

261 cm^{-2}, depicting the superior HER activity of Ni-P/BC. The Tafel slopes of Ni-P/FP

262 and Ni-P/GFP are respectively 230 mV dec^{-1} and 194 mV dec^{-1} (Figure 5e), which

263 indicates higher activation energy for HER [60]. Conversely Ni-P/BC possesses a

264 lower Tafel slope (140 mV dec^{-1}). EIS also demonstrated faster charge transfer for

265 Ni-P/BC, as indicated by its smaller semicircular diameter than Ni-P/FP and

266 Ni-P/GGP in Figure S10. The electrochemical surface area (ECSA) reflects the

267 number of active sites for electrodes and the value of ECSA is proportional to the

268 double-layer capacitance (C_{dl}) [61]. The C_{dl} values of these electrodes were

269 investigated by CV at different scan rates (Figure S11 and Figure 5f). It is noticeable

270 that compared with Ni-P/FP (3.9 mF cm^{-2}) and Ni-GFP (6.3 mF cm^{-2}), Ni-P/BC shows

271 a larger C_{dl} (10.2 mF cm^{-2}), implying again more active sites in Ni-P/BC. Therefore,

272 the remarkable HER activity of Ni-P/BC can be mainly attributed to the small size of

273 Ni-P particles on BC, increasing substantially the active surface area.[55, 56] It is

274 worth noting that Ni-P/BC also outperforms many reported non-precious metal HER

275 electrodes (Table S6-7). As we can note in Table S7, the substrates of electrodes

276 reported in the literature are conductive (such as glassy carbon, carbon paper, carbon

277 cloth, F-doped tin oxide and Ni foam), most of which are less economical and

278 environment-friendly than BC. In addition, ex situ prepared catalysts usually need to

be immobilized on conductive substrates with binders, which can impair the electrochemically active sites [24]. This makes the fabrication processes of electrodes more complex and expensive. Therefore, the binder-free Ni-P/BC electrode shows great advantages over these reported electrodes in terms of HER activity, cost, environment-friendliness and fabrication process.

Bi-metallic transition metal-phosphorous was also studied by introducing Co into Ni-P/BC (Figure S12). With the increment of Co incorporation, the particle aggregation tends to be more obvious and the overpotential becomes larger (Figure S13).

Finally, commercial Pt/C was also used as a comparison, coating it on carbon paper, since BC is not a conducting current collector. The overpotential of Ni-P/BC (161 mV) is indeed still higher than Pt/C (82 mV) at 10 mA cm^{-2} (Figure S14a). Although Pt/C shows better HER performance than Ni-P/BC, its durability is visibly poorer (Figure S14b), with a much more limited decrease of potential after 24 h for Ni-P/BC (~100 mV) than Pt/C (~310 mV). The cause of the dramatic deactivation of Pt/C is that phosphoric acid anions from PBS in the electrolyte can poison Pt [62]. Ni-P instead proves more robust in this neutral electrolyte.

4. Conclusion

In summary, a highly active freestanding and binder-free Ni-P hydrogen evolution catalyst supported on BC was obtained by electroless deposition. In terms of mechanical properties, pristine BC presents outstanding performance advantages over

301 carbonized BC. The deposition of Ni-P enables its use as electrode substrate. In fact, it

302 provides the required electric conductivity that is conventionally given by carbon

303 supports or additives. This can simplify the electrode preparation and decrease its cost.

304 Furthermore, Ni-P itself is a HER catalyst. Thus, in situ growth of Ni-P on BC not

305 only offers advantages of both Ni-P and BC, but also casts off the reliance on binders.

306 This novel Ni-P/BC catalyst working with a neutral electrolyte demonstrates superior

307 HER efficiency with a lower overpotential (161 mV) as compared to using Ni-P on

308 other substrates such as glass fiber paper (201 mV) or filter paper (252 mV)

309 highlighting the relevance of the specific nanoarchitecture of BC. Fibers of small

310 diameter are beneficial to form small-size particles leading to a more extended

311 catalytic active area. However, the outstanding performance also relies on the

312 electronic structure of the active sites. This is proven by the increased performance of

313 Ni-P, where a partial electron transfer from Ni to P occurs, compared with Ni-B,

314 where the transfer is from B to Ni. In a neutral phosphate buffer, not only Ni-P/BC

315 outperforms many reported non-precious metal HER electrodes, but it even shows

316 better stability than Pt/C. Considering the texture and conductivity of Ni-P/BC, our

317 strategy based on an electroless deposition process can also be promising in other

318 energy conversion and storage applications, such as water splitting, metal-air batteries

319 and supercapacitors.

320

321 **Declaration of competing interest**

322 The authors declare that they have no known competing financial interests or personal

relationships that could have appeared to influence the work reported in this paper.

References
[1] M.M. Rahman, E. Gemechu, A.O. Oni, A. Kumar. The greenhouse gas emissions' footprint and net energy ratio of utility-scale electro-chemical energy storage systems. Energy Convers Manage 2021;244:114497.
[2] A.M. Abdalla, S. Hossain, O.B. Nisfindy, A.T. Azad, M. Dawood, A.K. Azad. Hydrogen production, storage, transportation and key challenges with applications: A review. Energy Convers Manage 2018;165:602-27.
[3] Y. Ying, X. Luo, J. Qiao, H. Huang. "More is Different:" Synergistic Effect and

Structural Engineering in Double-Atom Catalysts. Adv Funct Mater 2020;31:2007423.

[4] Y. Li, G. Yang, S. Yu, Z. Kang, D.A. Talley, F.-Y. Zhang. Direct thermal visualization of micro-scale hydrogen evolution reactions in proton exchange membrane electrolyzer cells. Energy Convers Manage 2019;199:111935.

[5] Z. Wang, B. Xiao, Z. Lin, Y. Xu, Y. Lin, F. Meng, et al. $PtSe_2$/Pt Heterointerface with Reduced Coordination for Boosted Hydrogen Evolution Reaction. Angew Chem Int Edit 2021;60:23388-93.

[6] Z. Chen, X. Liu, T. Shen, C. Wu, L. Zu, L. Zhang. Porous NiFe alloys synthesized via freeze casting as bifunctional electrocatalysts for oxygen and hydrogen evolution reaction. Int J Hydrogen Energ 2021;46:37736-45.

[7] G.H. Gu, J. Lim, C. Wan, T. Cheng, H. Pu, S. Kim, et al. Autobifunctional Mechanism of Jagged Pt Nanowires for Hydrogen Evolution Kinetics via End-to-End Simulation. J Am Chem Soc 2021;143:5355–63.

[8] X. Tian, P. Zhao, W. Sheng. Hydrogen Evolution and Oxidation: Mechanistic Studies and Material Advances. Adv Mater 2019;31:1808066.

[9] O.A. Fakayode, B.A. Yusuf, C. Zhou, Y. Xu, Q. Ji, J. Xie, et al. Simplistic two-step fabrication of porous carbon-based biomass-derived electrocatalyst for efficient hydrogen evolution reaction. Energy Convers Manage 2021;227:113628.

[10] N. Dubouis, A. Grimaud. The hydrogen evolution reaction: from material to interfacial descriptors. Chem Sci 2019;10:9165-81.

[11] Y. Lei, Y. Wang, Y. Liu, C. Song, Q. Li, D. Wang, et al. Designing Atomic Active Centers for Hydrogen Evolution Electrocatalysts. Angew Chem Int Edit 2020;59:20794-812.

[12] C. Wang, L. Kuai, W. Cao, H. Singh, A. Zakharov, Y. Niu, et al. Highly dispersed Cu atoms in MOF-derived N-doped porous carbon inducing Pt loads for superior oxygen reduction and hydrogen evolution. Chem Eng J 2021;426:130749.

[13] G. Zhao, J. Chen, W. Sun, H. Pan. Non‐Platinum Group Metal Electrocatalysts toward Efficient Hydrogen Oxidation Reaction. Adv Funct Mater 2021;31:2010633.

[14] R. Wu, B. Xiao, Q. Gao, Y.R. Zheng, X.S. Zheng, J.F. Zhu, et al. A Janus Nickel Cobalt Phosphide Catalyst for High-Efficiency Neutral-pH Water Splitting. Angew Chem Int Edit 2018;57:15445-9.

[15] J. Wang, F. Xu, H. Jin, Y. Chen, Y. Wang. Non-Noble Metal-based Carbon Composites in Hydrogen Evolution Reaction: Fundamentals to Applications. Adv Mater 2017;29:1605838.

[16] T. Tronser, A. Laromaine, A. Roig, P.A. Levkin. Bacterial Cellulose Promotes Long-Term Stemness of mESC. ACS Appl Mater Interfaces 2018;10:16260-9.

[17] S. Roig-Sanchez, E. Jungstedt, I. Anton-Sales, D.C. Malaspina, J. Faraudo, L.A. Berglund, et al. Nanocellulose films with multiple functional nanoparticles in confined spatial distribution. Nanoscale Horiz 2019;4:634-41.

[18] Q. Xie, Z. Wang, L. Lin, Y. Shu, J. Zhang, C. Li, et al. Nanoscaled and Atomic Ruthenium Electrocatalysts Confined Inside Super-Hydrophilic Carbon Nanofibers for Efficient Hydrogen Evolution Reaction. Small 2021;17:2102160.

[19] X. Wang, Y. Fei, W. Zhao, Y. Sun, F. Dong. Tailoring unique neural-network-type

carbon nanofibers inserted in CoP/NC polyhedra for robust hydrogen evolution reaction. Nanoscale 2021;13:14705-12.

[20] Q. Kang, Y. Qin, Q. Lu, F. Gao. Waste leather-derived (Cr, N)-co-doped carbon cloth coupling with Mo2C nanoparticles as a self-supported electrode for highly active hydrogen evolution reaction performances. J Power Sources 2020;476:228706.

[21] Q. Xiong, Y. Wang, P.F. Liu, L.R. Zheng, G. Wang, H.G. Yang, et al. Cobalt Covalent Doping in MoS_2 to Induce Bifunctionality of Overall Water Splitting. Adv Mater 2018;30:1801450.

[22] S.-K. Park, J.K. Kim, Y.C. Kang. Amorphous Molybdenum Sulfide on Three-Dimensional Hierarchical Hollow Microspheres Comprising Bamboo-like N-Doped Carbon Nanotubes as a Highly Active Hydrogen Evolution Reaction Catalyst. ACS Sustainable Chem Eng 2018;6:12706-15.

[23] M. Park, D. Lee, S. Shin, H.J. Kim, J. Hyun. Flexible conductive nanocellulose combined with silicon nanoparticles and polyaniline. Carbohydr Polym 2016;140:43-50.

[24] X. Huang, X. Xu, C. Li, D. Wu, D. Cheng, D. Cao. Vertical CoP Nanoarray Wrapped by N,P-Doped Carbon for Hydrogen Evolution Reaction in Both Acidic and Alkaline Conditions. Adv Energy Mater 2019;9:1803970.

[25] Y. Yang, H. Gu, Q. Zhang, H. Li, H. Li. Ordered Mesoporous Ni-P Amorphous Alloy Nanowire Arrays: High-Efficiency Catalyst for Production of Polyol from Sugar. ACS Appl Mater Interfaces 2020;12:26101-12.

[26] D. Shin, H.J. Kim, M. Kim, D. Shin, H. Kim, H. Song, et al. $Fe_xNi_{2–x}P$ Alloy Nanocatalysts with Electron-Deficient Phosphorus Enhancing the Hydrogen Evolution Reaction in Acidic Media. ACS Catal 2020;10:11665-73.

[27] B. Lu, Y. Wang, W. Li, S. Song, P. Tian, R. Li, et al. Ni–P alloy@carbon nanotubes immobilized on the framework of Ni foam as a 3D hierarchical porous self-supporting electrode for hydrogen evolution reaction. Int J Hydrogen Energ 2021;46:23245-53.

[28] H. Li, L. Zhang, H. Lu, J. Ma, X. Zhou, Z. Wang, et al. Macro-/nanoporous Al-doped ZnO/cellulose composites based on tunable cellulose fiber sizes for enhancing photocatalytic properties. Carbohydr Polym 2020;250:116873.

[29] D.-H. Ha, B. Han, M. Risch, L. Giordano, K.P.C. Yao, P. Karayaylali, et al. Activity and stability of cobalt phosphides for hydrogen evolution upon water splitting. Nano Energy 2016;29:37-45.

[30] T. Meng, Y.N. Hao, L. Zheng, M. Cao. Organophosphoric acid-derived CoP quantum dots@S,N-codoped graphite carbon as a trifunctional electrocatalyst for overall water splitting and Zn-air batteries. Nanoscale 2018;10:14613-26.

[31] H. Li, P. Wen, D.S. Itanze, M.W. Kim, S. Adhikari, C. Lu, et al. Phosphorus-Rich Colloidal Cobalt Diphosphide (CoP_2) Nanocrystals for Electrochemical and Photoelectrochemical Hydrogen Evolution. Adv Mater 2019;31:1900813.

[32] W. Wang, S. Khabazian, S. Roig-Sanchez, A. Laromaine, A. Roig, D. Tonti. Carbons derived from alcohol-treated bacterial cellulose with optimal porosity for Li–O_2 batteries. Renew Energ 2021;177:209-15.

[33] L. Zhang, P. Zhu, F. Zhou, W. Zeng, H. Su, G. Li, et al. Flexible Asymmetrical

Solid-State Supercapacitors Based on Laboratory Filter Paper. ACS Nano 2016;10:1273-82.

[34] W. Hao, R. Wu, R. Zhang, Y. Ha, Z. Chen, L. Wang, et al. Electroless Plating of Highly Efficient Bifunctional Boride-Based Electrodes toward Practical Overall Water Splitting. Adv Energy Mater 2018;8:1801372.

[35] C.A. Schneider, W.S. Rasband, K.W. Eliceiri. NIH Image to ImageJ: 25 years of image analysis. Nat Methods 2012;9:671-5.

[36] J. Huang, Y. Su, Y. Zhang, W. Wu, C. Wu, Y. Sun, et al. FeOx/FeP hybrid nanorods neutral hydrogen evolution electrocatalysis: insight into interface. J Mater Chem A 2018;6:9467-72.

[37] D. Wang, Y. Zhang, X. Lu, Z. Ma, C. Xie, Z. Zheng. Chemical formation of soft metal electrodes for flexible and wearable electronics. Chem Soc Rev 2018;47:4611-41.

[38] M. Zeng, A. Laromaine, A. Roig. Bacterial cellulose films: influence of bacterial strain and drying route on film properties. Cellulose 2014;21:4455-69.

[39] Y. Yamauchi, T. Momma, T. Yokoshima, K. Kuroda, T. Osaka. Highly ordered mesostructured Ni particles prepared from lyotropic liquid crystals by electroless deposition: the effect of reducing agents on the ordering of mesostructure. J Mater Chem 2005;15:1987-94.

[40] Q. Yang, C. Lv, Z. Huang, C. Zhang. Amorphous film of ternary Ni-Co-P alloy on Ni foam for efficient hydrogen evolution by electroless deposition. Int J Hydrogen Energ 2018;43:7872-80.

[41] W. Hao, R. Wu, H. Huang, X. Ou, L. Wang, D. Sun, et al. Fabrication of practical catalytic electrodes using insulating and eco-friendly substrates for overall water splitting. Energy Environ Sci 2020;13:102-10.

[42] A. Sedighi, M. Montazer, S. Mazinani. Synthesis of wearable and flexible $NiP_{0.1}$-SnO_x/PANI/CuO/cotton towards a non-enzymatic glucose sensor. Biosens Bioelectron 2019;135:192-9.

[43] W. Tang, X. Liu, Y. Li, Y. Pu, Y. Lu, Z. Song, et al. Boosting electrocatalytic water splitting via metal-metalloid combined modulation in quaternary Ni-Fe-P-B amorphous compound. Nano Research 2020;13:447-54.

[44] S. He, Z. Li, H. Mi, C. Ji, F. Guo, X. Zhang, et al. 3D nickel-cobalt phosphide heterostructure for high-performance solid-state hybrid supercapacitors. J Power Sources 2020;467:228324.

[45] P. Zhang, M. Wang, Y. Yang, T. Yao, H. Han, L. Sun. Electroless plated Ni–B films as highly active electrocatalysts for hydrogen production from water over a wide pH range. Nano Energy 2016;19:98-107.

[46] Y. Wei, P. Zou, Y. Yue, M. Wang, W. Fu, S. Si, et al. One-Pot Synthesis of B/P-Codoped Co-Mo Dual-Nanowafer Electrocatalysts for Overall Water Splitting. ACS Appl Mater Interfaces 2021;13:20024-33.

[47] A. Chunduri, S. Gupta, O. Bapat, A. Bhide, R. Fernandes, M.K. Patel, et al. A unique amorphous cobalt-phosphide-boride bifunctional electrocatalyst for enhanced alkaline water-splitting. Appl Catal B 2019;259:118051.

[48] Q. Liu, H. Zhao, M. Jiang, Q. Kang, W. Zhou, P. Wang, et al. Boron enhances

oxygen evolution reaction activity over Ni foam-supported iron boride nanowires. J Mater Chem A 2020;8:13638-45.

[49] H. Li, H. Li, W.-L. Dai, W. Wang, J.-F. Deng. XPS studies on surface electronic characteristics of Ni–B and Ni–P amorphous alloy and its correlation to their catalytic properties. Appl Surf Sci 1999;152:25-34.

[50] Y. Kang, J. Henzie, H. Gu, J. Na, A. Fatehmulla, B.S.A. Shamsan, et al. Mesoporous Metal-Metalloid Amorphous Alloys: The First Synthesis of Open 3D Mesoporous Ni-B Amorphous Alloy Spheres via a Dual Chemical Reduction Method. Small 2020;16:1906707.

[51] L. Wan, Y. Wang, Y. Zhang, C. Du, J. Chen, Z. Tian, et al. FeCoP nanosheets@Ni-Co carbonate hydroxide nanoneedles as free-standing electrode material for hybrid supercapacitors. Chem Eng J 2021;415:128995.

[52] Q. Liu, J. Tian, W. Cui, P. Jiang, N. Cheng, A.M. Asiri, et al. Carbon nanotubes decorated with CoP nanocrystals: a highly active non-noble-metal nanohybrid electrocatalyst for hydrogen evolution. Angew Chem Int Edit 2014;53:6710-4.

[53] K. Wang, K. Sun, T. Yu, X. Liu, G. Wang, L. Jiang, et al. Facile synthesis of nanoporous Ni–Fe–P bifunctional catalysts with high performance for overall water splitting. J Mater Chem A 2019;7:2518-23.

[54] F. Li, Y. Li, Q. Zhuo, D. Zhou, Y. Zhao, Z. Zhao, et al. Electroless Plating of NiFeP Alloy on the Surface of Silicon Photoanode for Efficient Photoelectrochemical Water Oxidation. ACS Appl Mater Interfaces 2020;12:11479-88.

[55] X. Chen, D. Wang, Z. Wang, P. Zhou, Z. Wu, F. Jiang. Molybdenum phosphide: a new highly efficient catalyst for the electrochemical hydrogen evolution reaction. Chem Commun 2014;50:11683-5.

[56] D. Liu, X. Li, S. Chen, H. Yan, C. Wang, C. Wu, et al. Atomically dispersed platinum supported on curved carbon supports for efficient electrocatalytic hydrogen evolution. Nat Energy 2019;4:512-8.

[57] X. Xie, M. Song, L. Wang, M.H. Engelhard, L. Luo, A. Miller, et al. Electrocatalytic Hydrogen Evolution in Neutral pH Solutions: Dual-Phase Synergy. ACS Catal 2019;9:8712-8.

[58] L. Ren, D. Yang, J.-H. Yang. Ruthenium-manganese phosphide nanohybrid supported on graphene for efficient hydrogen evolution reaction in acid and alkaline conditions. Int J Hydrogen Energ 2022;47:13876-86.

[59] X. Li, L. Zhang, Z. Wang, S. Wu, J. Ma. Cellulose controlled zinc oxide nanoparticles with adjustable morphology and their photocatalytic performances. Carbohydr Polym 2021;259:117752.

[60] H. Li, S. Lu, J. Sun, J. Pei, D. Liu, Y. Xue, et al. Phase-Controlled Synthesis of Nickel Phosphide Nanocrystals and Their Electrocatalytic Performance for the Hydrogen Evolution Reaction. Chemistry-A European Journal 2018;24:11748-54.

[61] S. Shen, Z. Lin, K. Song, Z. Wang, L. Huang, L. Yan, et al. Reversed Active Sites Boost the Intrinsic Activity of Graphene-like Cobalt Selenide for Hydrogen Evolution. Angew Chem Int Edit 2021;60:12360-5.

[62] Y. Tan, M. Luo, P. Liu, C. Cheng, J. Han, K. Watanabe, et al. Three-Dimensional Nanoporous $Co_9S_4P_4$ Pentlandite as a Bifunctional Electrocatalyst for Overall Neutral

525   Water Splitting. ACS Appl Mater Interfaces 2019;11:3880-8.
526